

## ●Original Contribution

PERFORMANCE OF A MINIATURE MAGNETIC POSITION SENSOR  
FOR THREE-DIMENSIONAL ULTRASOUND IMAGINGDANIEL F. LEOTTA,\* PAUL R. DETMER<sup>†</sup> and ROY W. MARTIN\*<sup>‡</sup>\*Center for Bioengineering and Departments of <sup>†</sup>Surgery and <sup>‡</sup>Anesthesiology,  
University of Washington, Seattle, WA, USA

(Received 23 August 1996; in final form 10 December 1996)

**Abstract**—A miniature magnetic position sensor used for three-dimensional ultrasound imaging was tested for precision and accuracy *in vitro*. The sensor alone was able to locate points with root-mean-square (rms) uncertainty of 1.7 mm and accuracy of  $0.05 \pm 0.62$  mm over its specified operating range of 50 cm. With an ultrasound imaging system, a point was located from arbitrary viewing windows with 2.4-mm rms uncertainty and  $0.06 \pm 0.68$  mm accuracy. If viewing windows were limited to those representative of a typical ultrasound examination, the system could achieve rms uncertainty in point location of  $< 1$  mm. Performance was not affected by operation of the imaging system when the sensor was mounted on an ultrasound scanhead. Sensitivity to metals in the operating environment was also measured. © 1997 World Federation for Ultrasound in Medicine & Biology.

**Key Words:** Ultrasound, Imaging, Three-dimensional, Magnetometer, Position, Orientation.

## INTRODUCTION

Quantitative three-dimensional (3D) ultrasound imaging depends on the accurate registration of multiple two-dimensional (2D) image planes in a 3D coordinate system. A number of systems that are designed to link 3D position and orientation information to an ultrasound scan plane have been reported. Approaches include acoustic location (Handschumacher et al. 1993; King et al. 1990), mechanically controlled scanners (Martin et al. 1990; Roelandt et al. 1994), optical tracking (Stone 1990; Trobaugh et al. 1994) and magnetic location (Detmer et al. 1994; Riccabona et al. 1995). These techniques have been used recently to explore clinical applications of 3D ultrasound scanning. Estimates of ventricular volume both *in vitro* and *in vivo* have been reported based on acoustic location (Jiang et al. 1995; Sapin et al. 1993, 1994). Gilja et al. (1994, 1995) used a mechanically tilted transducer to make volume estimates of abdominal organs *in vitro* and *in vivo*. Atherosclerotic plaque volumes were quantified with a linearly scanned system (Delcker and Diener 1994). Magnetic systems have been described

for fetal (Kelly et al. 1994; Pretorius and Nelson 1994) and vascular (Hodges et al. 1994) 3D imaging.

Magnetic tracking techniques avoid several problems associated with other 3D location systems. The major drawback of mechanical systems is their limited range of motion, which may restrict acquisition to parallel planes or planes rotated about a fixed pivot point. Techniques that instead provide multiple intersecting scanning planes may enhance the coverage of structures of interest and increase the accuracy of subsequent 3D reconstructions. Magnetic tracking permits free transducer movement, allowing acquisition of arbitrarily oriented 2D images from one or more acoustic windows. A disadvantage of the acoustic and optical systems is the requirement of a direct line of sight between the sensing equipment (microphones, cameras) and the ultrasound scanhead. In contrast, magnetic systems do not impose restrictions on transducer placement during scanning. Magnetic location performance is also independent of scanhead orientation when the system operates within the rated range, unlike the acoustic spark-gap system. The major constraint on magnetic tracking is the need to maintain an imaging environment that is free of ferromagnetic materials.

The devices mounted on the scanhead for acoustic, optical or magnetic tracking are often bulky and

Address correspondence to: Daniel F. Leotta, Center for Bioengineering, University of Washington, Box 357962, Seattle, WA 98195, USA.

can interfere with normal scanning procedures. Some applications, such as 3D localization of a transesophageal imaging probe, require a sensor that is significantly smaller than those previously described. A miniature magnetic sensor, similar to the one evaluated by Detmer et al. (1994), has recently become available. Preliminary precision results with prototypes of the miniature sensor have been reported previously (Leotta et al. 1995; Martin et al. 1993). In the present study, we have evaluated the 3D point localization capability of an upgraded version of the sensor. Specific goals were to: (1) measure the precision and accuracy of the miniature sensor as a function of distance from the transmitter, both independent of and in conjunction with an ultrasound imaging system; (2) measure the effects of ultrasound imaging equipment and metals in the environment on the performance of the magnetic locating system; and (3) establish a procedure for consistent system calibration.

## METHODS

### *Magnetic location system*

We used a commercial magnetic 6D position and orientation measurement system (Flock of Birds model 6DFOB, Ascension Technology Corp., Burlington, VT, USA) to track an ultrasound scanhead for 3D imaging. The system includes a magnetic field generator (transmitter), a magnetic sensor (receiver) and an electronic control unit. Three orthogonal receiving coils sense orthogonal pulsed DC magnetic fields generated sequentially by the transmitter. These measurements are used to compute the receiver's position and orientation in space with respect to the origin of the transmitter. The receiver position is reported as  $x$ ,  $y$  and  $z$  coordinates relative to the transmitter. A  $3 \times 3$  matrix of angle cosines defines the orientation of the receiver axes with respect to the transmitter axes. The relationship between the coordinate systems of the transmitter and receiver is shown in Fig. 1.

The miniature receiver package measures  $17 \times 8 \times 8$  mm, while the standard-sized unit is  $25.4 \times 25.4 \times 20$  mm (Fig. 2). The miniature sensor is also available without the plastic covering shown in Fig. 2, which reduces the sensor size to  $9 \times 6 \times 6$  mm. The manufacturer-specified operating range of the miniature receiver is 50 cm, measured radially from the transmitter, compared with the 91-cm range of the standard receiver.

Several features of the Ascension Technology design enhance the system's performance and flexibility. (1) The pulsed DC magnetic fields are less susceptible than AC magnetic fields to errors resulting from eddy currents in conducting materials near the receiver.

Therefore, the receiver can be placed directly on an ultrasound scanhead. (2) The ambient magnetic field is measured after each cycle and subtracted from the preceding measurements, before the receiver position and orientation are calculated. This technique compensates for constant or slowly varying field distortions in the operating environment. (3) The system measurement rate can be varied from 16–144 Hz, and internal filters are included (an AC filter to eliminate low-frequency sinusoidal signals and a DC lowpass filter) whose characteristics can be adjusted by the user. Changes in measurement rate and filtering parameters can tune the system for a particular application or operating environment.

Two approaches have been taken to assess the performance of the miniature magnetic sensor. First, to measure the performance of the location system alone, the sensor was mounted on a stylus as shown in Fig. 3(a). Second, to study the performance of a 3D ultrasound imaging system based on this magnetic location system, the sensor was mounted on a scanhead as shown in Fig. 3(b). Point localization tests using these two configurations are described separately below. Several of the tests were repeated using the latest model of the standard sensor, to provide a direct comparison between the two sensor designs.

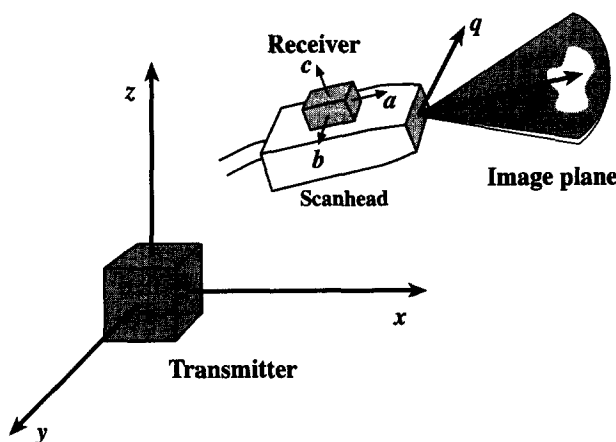


Fig. 1. Definition of the coordinate systems of the magnetic field generator (transmitter), the magnetic field sensor (receiver) and the ultrasound image plane. The magnetic location system determines the spatial relationship between the transmitter and the receiver, returning three translational components and a  $3 \times 3$  matrix of direction cosines that relates the receiver axes ( $a, b, c$ ) to the transmitter axes ( $x, y, z$ ). The calibration procedure defines the spatial relationship between the imaging plane and the receiver, returning three translational components and a  $2 \times 3$  matrix of direction cosines that relates the image row and column axes ( $r, q$ ) to the receiver axes ( $a, b, c$ ). These relationships can be used to map any image pixel address to a 3D location in the transmitter's coordinate system.



Fig. 2. Photograph of the miniature magnetic sensor both alone (lower left) and mounted on a 5- to 3-MHz phased array ultrasound scanhead (center). A custom-designed plastic holder has been glued on the scanhead, into which the sensor can be inserted. The sensor can be removed from the fitting and replaced precisely in the same position, allowing transfer of a single sensor to different scanheads. A standard sensor is shown for size comparison (upper right).

### Three-dimensional location system performance

The precision and accuracy of the magnetic sensor were first evaluated independent of the ultrasound imaging system. The precision is the ability to locate repeatably the same point in space, while the accuracy is the ability to measure the true position of the point. All tests were conducted with the sensor mounted on the ultrasound scanhead used in subsequent imaging tests (Fig. 2). However, the scanhead was disconnected from the imager for all tests except those explicitly designed to study potential electromagnetic interference associated with the imaging equipment. Extraneous metals were kept at least 1 m from the transmitter and receiver during data collection except during specific tests of interference due to metals.

Position and orientation data were collected at a receiver measurement rate of 106.5 Hz unless otherwise specified. This rate is near the system default operating rate of 103.5 Hz. The specific sampling rate was chosen by comparing noise measurements over a range of operating frequencies in the laboratory environment and choosing a rate within a region of relatively low noise. For instance, in the United States, noise is higher at frequencies that are integral multiples or submultiples of 60 Hz (the power line frequency), and measurement rates at or near these frequencies should be avoided.

Receiver position and orientation measurements were recorded on a 486 computer under the control of custom software designed with LabView (National Instruments Corp., Austin, TX, USA). Numerical calcula-

tions were performed with MATLAB (The MathWorks, Inc., Sherborn, MA, USA) on the same computer.

**Precision.** The precision of the magnetic location system was measured by attaching the receiver/scanhead combination to a plastic stylus and using multiple readings of position and orientation to locate a fixed pivot point in space (Fig. 3(a)). The 3D location of the pivot point relative to the transmitter can be determined if the spatial relationship between the receiver and the stylus pivot point is known. For an ideal system, the computed point location would not change from sample to sample. However, noise in the sensor measurements leads to variability in the computed location of the pivot point. The resulting root-mean-square (rms) uncertainty around the mean point location is used as the measure of the system's precision.

The actual distance from the receiver to the pivot point could not be measured directly, since the receiver packaging encloses its origin and there are no external reference marks. Therefore, the vector relating the receiver location to the stylus pivot point was determined

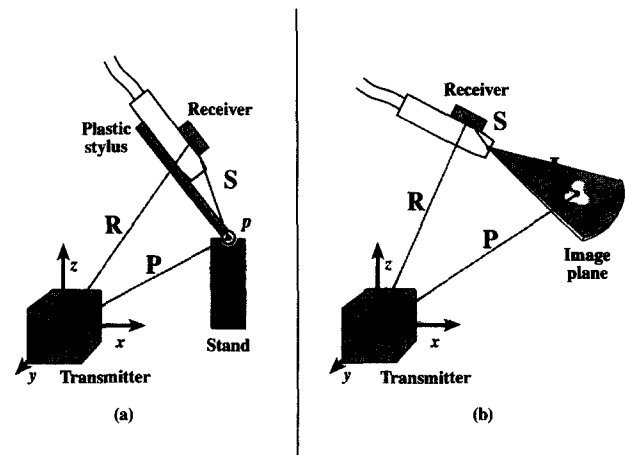


Fig. 3. Diagram of the vector relationship between the transmitter, receiver and point of interest for stylus and imaging tests. (a) The receiver/scanhead combination is attached to the plastic stylus and rotated about the pivot point  $p$ . The vector  $P$  (the 3D location of the pivot point) is the sum of the receiver measurement  $R$  and the calibration vector  $S$ . A small bead (6-mm diameter) keeps the stylus seated in the pivot point (a plastic ring on a wooden stand) during sampling. (b) A point of interest  $p$  is chosen in an ultrasound image plane. The vector  $P$  (the 3D location of the image point) is the sum of the receiver position  $R$ , the calibration vector  $S$  and the image plane distance  $I$ . The imaging calibration procedure determines both  $S$  and the  $2 \times 3$  matrix of direction cosines that defines the orientation of the image plane relative to the receiver. The vector  $I$ , a 2D vector that lies in the image plane, is computed by converting the target location from a pixel address to a distance from the scanhead center.

by the following calibration procedure. The stylus was rotated to 32 different positions distributed in a hemispherical pattern around the pivot point. An iterative least-squares fitting technique (Detmer et al. 1994) was applied to find the vector from the receiver to the pivot point (**S** in Fig. 3(a)), which minimized the scatter in the pivot point's 3D location (**P** in Fig. 3(a)). This procedure was repeated for three different pivot points located 250–300 mm from the transmitter. The vectors computed from these three initial runs were averaged to provide a single calibration vector for subsequent precision measurements.

Tests to determine the pivot point location relative to the transmitter were performed over a distance range of 100–800 mm from the transmitter. Pivot points were located at nine distances along each of the three transmitter axes ( $x$ ,  $y$ ,  $z$ ). Thirty-two position and orientation measurements were made around each point. The pivot point location was computed for each of the 32 sample points using the mean calibration vector. The mean of the computed point location was found, and the vector sum of the standard deviations in  $x$ ,  $y$  and  $z$ , around the mean provided the rms uncertainty in the point location. The rms uncertainty measured for each of the three coordinate axes was averaged at each distance. Identical tests were performed with a standard-sized receiver for comparison.

**Accuracy.** System accuracy was measured by moving the receiver over a set of grid points on a pegboard and comparing interpoint distances measured by the location system with those measured by micrometer. The deviation of the sensor measurements from the known distances is used as the measure of system accuracy. It was necessary to compare distances between points rather than absolute distances since the physical origin of the transmitter was not accessible.

The receiver/scanhead combination was attached to a plastic block and moved over a  $6 \times 2$  planar grid, with points separated by 76.2 mm (3 inches). The grid was oriented such that the receiver was moved away from the transmitter, along either the  $x$ -,  $y$ - or  $z$ -axis of the transmitter coordinate system. The distance from the transmitter to the receiver varied from 100–550 mm. Measurements across the grid were made three times along each axis. Differences in sensor location were compared with the known distance between the grid points. Distances were computed between the three measured locations for each grid point and each of the three measured locations of the adjacent points; the differences from the true distance were averaged for the three axes.

**Interference: Imaging mode.** The potential effect of ultrasound equipment operation on the location system's performance is a major concern when a magnetic locating device is used. To study the effect of electrical noise generated by the ultrasound system in its different operating modes, precision and accuracy measurements were made with the ultrasound machine turned off, and with the machine running in B-mode, color Doppler and duplex Doppler modes. The ultrasound instrument was located approximately 1 m from the transmitter during these tests.

Precision was measured as described above by locating a point with the receiver/scanhead attached to a stylus. Three runs of 32 measurements each were made at each of two distances from the transmitter (200 and 400 mm along the  $x$ -axis) for each of the four operating modes. Two-sample  $F$ -tests for equal variance were performed on data collected with the imager switched off and in each of the three operating modes. Accuracy was measured as described above by moving the receiver over a set of grid points on a pegboard. Measurements were made three times along the  $x$ -axis of the transmitter for each of the four operating modes. The mean difference from the true distance was calculated for each case and two-sample  $t$ -tests for equal means were performed on the results with and without the imaging system in use.

**Interference: Metals.** Any magnetic locating system is susceptible to interference from metals in the immediate vicinity. The effects depend on the characteristics of the particular metal, and in some cases measurement rate adjustments can be made to minimize interference. Ferromagnetic metals, characterized by high magnetic permeability, are expected to degrade system performance at all measurement rates due to distortions of the transmitter's magnetic fields. Metals such as stainless steel (low permeability and low conductivity) are not expected to affect performance at any measurement rate. Low-permeability, high-conductivity metals (such as aluminum) can introduce errors due to eddy currents, which are induced in the metal by changes in the magnetic field. In this case, a lower system measurement rate can be selected to allow the eddy currents to subside and thereby reduce location measurement errors.

The precision of the magnetic tracking system was measured in the presence of metals, using both a high (106.5 Hz) and low (26.5 Hz) measurement rate. The low measurement rate was selected by comparing noise measurements from 16–30 Hz and choosing an appropriate rate as described above. The amount of DC signal filtering was increased for the low measurement rate rela-

tive to the default system settings used at the high measurement rate, and AC filtering was turned off.

Measurements were first taken at the high and low measurement rates without any metals present. Data were collected with the stylus as detailed above, at distances of 200–550 mm from the transmitter. The test was then repeated with three separate metals: aluminum (140 g), stainless steel (35 g) and a ferromagnetic surgical clamp (30 g). The aluminum and stainless steel samples were attached alongside the receiver mount, while the surgical clamp was attached on the opposite side of the stylus (50 mm from the receiver) since the system will not operate with ferromagnetic material immediately adjacent to the receiver.

### *Three-dimensional imaging performance*

The magnetic location system was next tested in conjunction with an ultrasound imaging system. The imaging probe used in all tests was a broadband 5- to 3-MHz phased array sector-scan ultrasonic scanhead. The probe was connected to an HDI 3000 imager (Advanced Technology Laboratories, Inc., Bothell, WA, USA). Images and location data were collected using an ImageVue workstation (Nova Microsonics, Inc., Mahwah, NJ, USA) under the control of a 486 computer running custom-designed LabView software. Off-line identification of points of interest in the images was performed using NIH Image software (National Institutes of Health, Bethesda, MD, USA) on a Macintosh IIfx computer (Apple Computer, Inc., Cupertino, CA, USA).

**Calibration.** The spatial relationship between the magnetic receiver and the image plane must be known to achieve accurate 3D ultrasound imaging. An iterative calibration technique (an extension of the method used above) established the relative position and orientation of the receiver and the image plane (Detmer *et al.* 1994). The algorithm returned the position offsets ( $a$ ,  $b$ ,  $c$ ) from the receiver origin to the image sector origin ( $S$  in Fig. 3(b)), and a  $2 \times 3$  matrix of angle cosines, which defines the orientation of the image row and column axes with respect to the three receiver coordinate axes. The calibration data map the points in the ultrasound image plane to the coordinate system of the receiver. The sensor measurements then map the image point locations to the coordinate system of the transmitter.

The calibration procedure is based on multiple images of a point target captured over a range of transducer locations and orientations. The target was a brass sphere (1.5-mm diameter) suspended by a thread in a water tank, which provided an easily visualized fixed

point in the ultrasound images. Two cylindrical plastic tanks (diameters of 12 and 15 cm) were used for the calibration. Both tanks were made of thin (thickness  $< 1$  mm), semiflexible, high-density polyethylene. The transmitter was located 15–20 cm beneath the target.

A single calibration data set consisted of 32 images collected for receiver positions uniformly distributed in the transmitter  $x$ - $y$  plane with arbitrary orientations (the tank design limited the variation in the  $z$ -direction). The target was imaged directly through the wall of the water tank and from the surface of the water, with the ultrasound probe held by hand. The target was centered in the ultrasound beam thickness by tilting the transducer until the point target appeared brightest. Lateral target location in the image sector was varied as much as possible by manipulation of the transducer. Maximum imaging depth was set to 8.7 cm for the smaller tank and 11.6 cm for the larger tank. The two water tanks produced point target locations at different distances from the transducer face (3–6 cm for the smaller tank, 5–9 cm for the larger tank).

The row and column pixel coordinates of the target location on each image were recorded off-line. The target coordinates were converted from pixels to millimeters, with adjustments made for the speed of sound in water and sector angle distortions, and then passed to the calibration software with the corresponding receiver location data. The calibration algorithm iteratively searched for the position and orientation of the receiver with respect to the image plane by minimizing the scatter of the calculated target position ( $P$  in Fig. 3(b)) in the transmitter's coordinate system.

A total of six calibration data sets were collected, three from each of the two tanks. A single calibration matrix was found by combining the six individual data sets into a single set and finding the overall best-fit transformation matrix. Since the target position relative to the transmitter was not necessarily the same for each image set (as required by the calibration algorithm), the data were first transformed to a common origin. The mean location of the point target for each calibration set, returned by an initial run of the calibration program, was subtracted from the magnetic sensor location readings. Application of the calibration algorithm to this composite data set produced the final calibration matrix. A standard-sized receiver was also calibrated with this scanhead for comparison.

Calibration matrices were computed using subsets of the full data set to assess the effect of the imaging depth on the consistency and accuracy of the result. In addition to the six individual matrices computed above, three more calibration matrices were computed by combining independent pairs of data sets, with the two sets

in each pair collected at different imaging depths. The range of each of the calibration offset values ( $a$ ,  $b$ ,  $c$ ) was found for: (1) the three matrices computed for the smaller depth (8.7 cm), (2) the three matrices computed for the larger depth (11.6 cm), and (3) the three matrices computed from the paired data sets.

Calibration matrices that more accurately describe the relationship between the receiver and the image plane are expected to achieve better precision in independent point-target imaging tests. Eight additional sets of images were collected with several instrument depth settings (10–14 cm) in several different plastic containers. The six individual calibration matrices, the three paired-set matrices and the final matrix were used to reconstruct the 3D position of the point target. For each matrix, the rms uncertainty in the target position was computed for each of the eight image sets and the results were averaged. The mean rms uncertainty was found for the three matrices computed for the smaller imaging depth, the three matrices computed for the larger imaging depth and the three matrices computed from the paired data sets.

**Precision.** Precision of the imaging system was compared for several image collection protocols, designed to simulate common ultrasound imaging procedures. Precision was measured as described above by imaging a point target and calculating the rms uncertainty in its computed 3D location. First, the transducer was aligned with the  $x$ -axis of the transmitter and rotated to two orthogonal orientations (image plane parallel to the  $x$ - $y$  plane and parallel to the  $x$ - $z$  plane), simulating long- and short-axis views of an organ from one imaging window (Fig. 4). Sixteen images were captured for each orientation, with transducer tilt and  $z$ -position varied between images. This procedure was then repeated for a second viewing window aligned with the  $y$ -axis of the transmitter. Finally, the target was imaged twice with 32 arbitrary transducer positions and orientations. All image sets were collected using the larger plastic cylinder, and the final calibration matrix was used to calculate the location of the target in the transmitter coordinate system.

The data collected with limited transducer movement were grouped to simulate three scanning protocols: (1) one window and one orientation, (2) one window and two orientations, and (3) two windows and two orientations. The precision for each of these three protocols was computed as: (1) the mean rms uncertainty of the four individual image sets, (2) the mean rms uncertainty of the 32 images collected at each viewing location, and (3) the rms uncertainty for all 64 images. For a fourth protocol, the mean rms uncertainty was computed

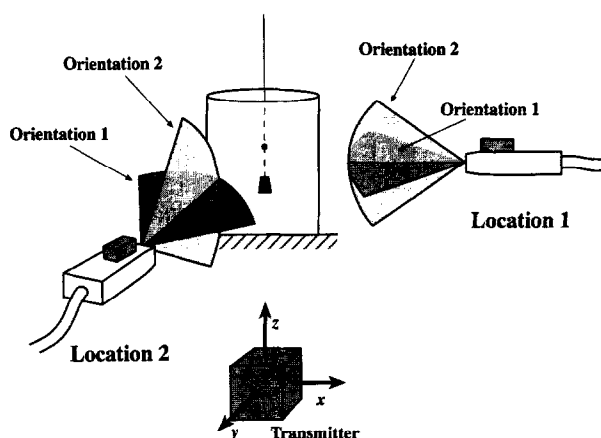


Fig. 4. Diagram of the imaging protocols used to assess imaging precision. The bead target was imaged through the wall of a plastic tank from two different windows (Locations 1 and 2) with two orthogonal image plane orientations (Orientations 1 and 2). The brass bead target is shown suspended by a thread in the plastic tank; a nonmagnetic weight at the end of the thread stabilized the bead position in the water.

for the two image sets collected with arbitrary transducer position and orientation.

Precision as a function of transmitter distance was measured by imaging a single point target with transmitter locations ranging from directly beneath the target to a distance of 550 mm. For each transmitter location, 16 images of the target were collected from one window with a single transducer orientation.

Precision was measured as a function of target depth in the image by successively moving the target away from the transducer, while the transmitter and tank positions were held constant. The maximum imaging depth setting was varied from 5.7–17.6 cm, with target distances ranging from 4–16 cm from the scan-head face. At each depth setting, the focal zone was set to its maximum depth and the target was positioned at or proximal to the focus. Sixteen images were collected at each depth setting, from one window with a single transducer orientation.

**Accuracy.** A phantom consisting of a  $4 \times 2$  planar grid of equally spaced beads (25.0-mm separation) was imaged in a water bath to assess the accuracy of the imaging system. Each bead was imaged with four different transducer orientations (transducer facing the  $\pm x$  axes and the  $\pm y$  axes of the transmitter coordinate system). The phantom was imaged twice at each of two different instrument depth settings (8.7 and 12.4 cm), with the transmitter centered 250–300 mm beneath the phantom. Distances were computed between the four measured locations of each bead and the four measured locations

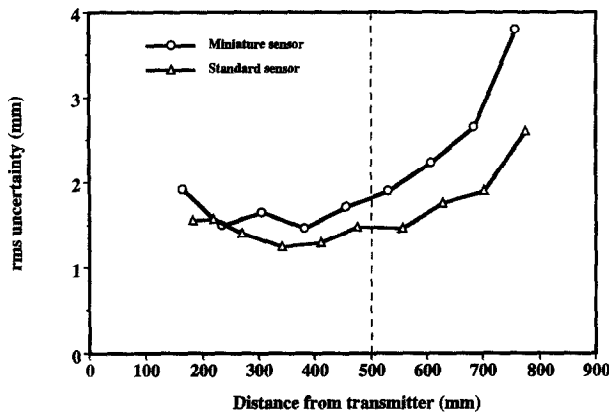


Fig. 5. Comparison of precision as a function of pivot point distance from the transmitter for the miniature and standard sensors alone. Each plotted point represents the mean rms uncertainty in pivot point location as determined by stylus tests along each of the three coordinate axes (32 samples/test). The dashed line at 500 mm represents the manufacturer's specified maximum range of the miniature sensor. The standard sensor's maximum specified range is 910 mm.

of each adjacent bead (total of 160 differences for each run). The distances were compared to the true distances, as measured with a micrometer.

Accuracy as a function of transmitter distance was measured by imaging the bead phantom with transmitter locations ranging from directly beneath the phantom to a distance of 550 mm. Each bead was imaged with one transducer orientation for each transmitter location, and distances between adjacent beads were computed and compared with the measured distances.

## RESULTS

### Three-dimensional location system performance

**Precision.** The mean vector magnitude from the stylus point to the receiver was 106 mm for the three calibration data sets. The precision of the sensor as a function of distance is shown in Fig. 5. The measured precision of the standard-sized sensor is included for comparison. Over the nominal operating range of the miniature sensor ( $< 500$  mm) the precision was nearly equal for the two sensors (mean rms uncertainty 1.7 mm for the miniature sensor, 1.4 mm for the standard sensor). In the 500- to 800-mm range, the performance of the miniature sensor degraded (mean rms uncertainty 2.6 mm for the miniature sensor, 1.9 mm for the standard sensor).

**Accuracy.** The mean differences between the miniature sensor readings and the true distances across the

grid are shown in Fig. 6. Over the operating range of the system, the accuracy was  $0.05 \pm 0.62$  mm (mean  $\pm$  standard deviation).

**Interference: Imaging mode.** Precision of the magnetic tracking system was not degraded by the ultrasound operating mode at either the near or far location of the stylus pivot point (Fig. 7(a)). The rms uncertainty, averaged over the six stylus data sets, varied by 0.1 mm for the four operating modes. The *F*-tests indicated no significant differences in variance except in the color Doppler mode, for which variance was significantly lower ( $p < 0.02$ ). Accuracy was also unaffected by the operating mode (Fig. 7(b)), with the mean difference from the true distance within  $\pm 0.1$  mm in all cases. The *t*-tests produced a minimum *p* value of 0.3, indicating no statistical difference between means.

**Interference: Metals.** With no metal present, the precision of the system was better for the higher measurement rate (mean rms uncertainty 1.7 mm for the high rate, 2.0 mm for the low rate) (Fig. 8). However, when a piece of aluminum was attached to the stylus, the precision at the higher measurement rate degraded markedly (mean rms uncertainty 4.3 mm), while the precision at the lower rate did not change. Stainless steel had no effect on performance at either the high or low measurement rate, while ferromagnetic material degraded performance at both measurement rates.

### Three-dimensional imaging performance

**Calibration.** The variability in point target location for the calibration data is summarized in Table 1. The

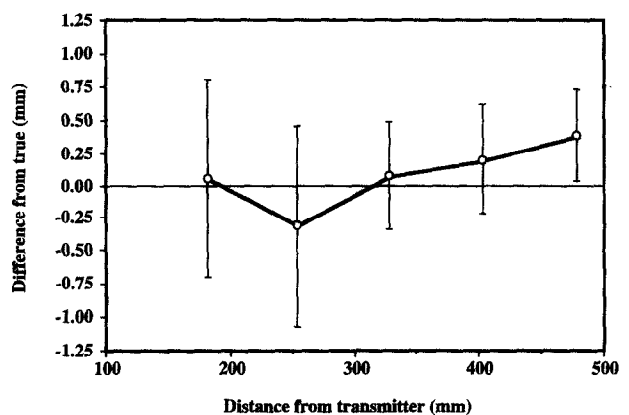


Fig. 6. Mean difference between the length measured by the miniature sensor alone and the true length as a function of distance from the transmitter for measurements along a grid. The bars represent the standard deviations for 108 measurements at each distance.

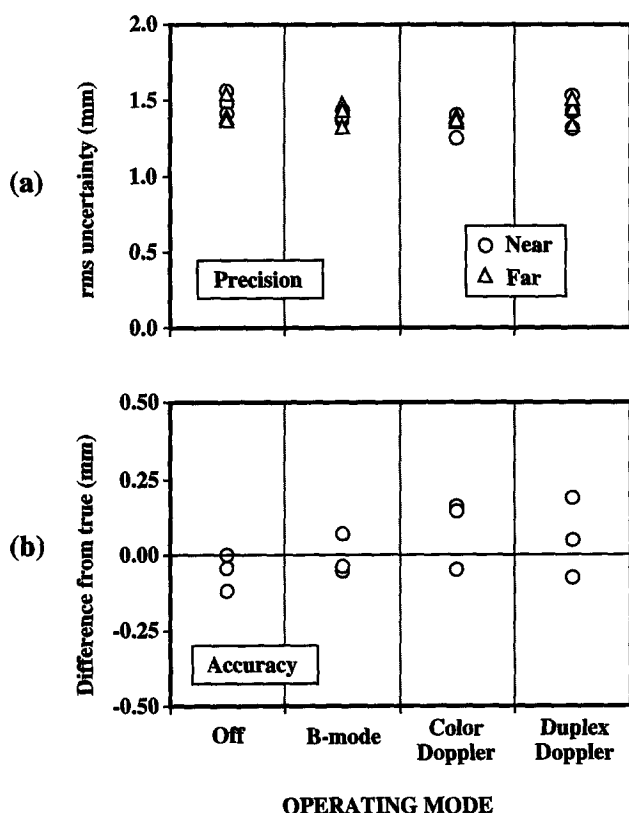


Fig. 7. Comparison of precision and accuracy of the miniature sensor alone for different ultrasound instrument operating modes. (a) Precision is shown as the rms uncertainty in point location for three separate stylus tests at two distances from the transmitter (Near = 200 mm, Far = 400 mm). (b) Accuracy is shown as the difference between the sensor length measurement and the true length for three separate tests along a grid.

overall rms uncertainty in the point target location for the full calibration data set was 2.4 mm. In comparison, the rms uncertainty in point target location with the imaging system for a standard sensor on the same scanhead was 2.1 mm.

The variability in the estimates of the calibration matrix produced by the data sets from a single imaging depth were compared with those produced by the paired sets from different depths. Figure 9 shows the range of the position offsets ( $a$ ,  $b$ ,  $c$ ) of the calibration matrices derived for each imaging depth (8.7 and 11.6 cm) and for the paired data sets. Note the large variability of the matrices derived for the smaller depth (22.7-mm maximum range) compared with those for the larger depth (5.9-mm maximum range). The combined data sets collected at different depths produced the most consistent estimate of the calibration matrix (2.2-mm maximum range).

The relative accuracy of the calibration matrices was assessed by comparing the rms uncertainty in 3D point

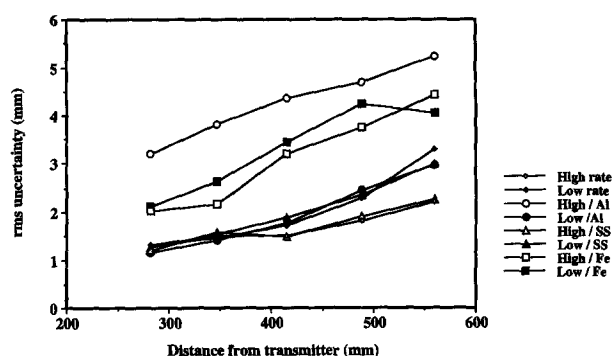


Fig. 8. Comparison of sensor precision for high (106.5 Hz) and low (26.5 Hz) system measurement rates in the presence of metals (Al = aluminum; SS = stainless steel; Fe = ferromagnetic clamp). With no metal present, the rms uncertainty increases for the low rate compared with the high rate. Aluminum in the operating environment degrades performance at the high rate but not at the low rate. Stainless steel does not affect performance at either rate, and ferromagnetic material degrades performance at both rates.

target location computed for eight additional image sets. Precision is shown in Fig. 10 for the three groups of matrices compared in Fig. 9 and for the final calibration matrix. The mean rms uncertainty decreased dramatically for the 11.6-cm-depth data set (2.5 mm) compared with the 8.7-cm-depth set (3.9 mm). Mean performance for the matrices derived from the paired data sets (2.28-mm rms uncertainty) was nearly equivalent to that for the final matrix derived from the six combined data sets (2.26-mm rms uncertainty).

**Precision.** The measurements of precision in point target location for four scanning protocols, computed by using the final calibration matrix to reconstruct images of a single point, are compared in Fig. 11. Scanning complexity increased from protocol 1 (limited transducer position and orientation) to protocol 4 (arbitrary position and orientation). Precision degraded

Table 1. Point target location results for the final calibration matrix, based on a total of 192 images collected at two imaging depths.

Std deviation $x$ (mm)	1.53
Std deviation $y$ (mm)	1.41
Std deviation $z$ (mm)	1.20
Range $x$ (mm)	6.53
Range $y$ (mm)	6.09
Range $z$ (mm)	5.77
rms uncertainty (mm)	2.41

The standard deviations are measured around the mean point target location and the ranges are the differences between the maximum and minimum deviations from the mean. The rms uncertainty is the vector sum of the standard deviations in the  $x$ ,  $y$  and  $z$  directions.



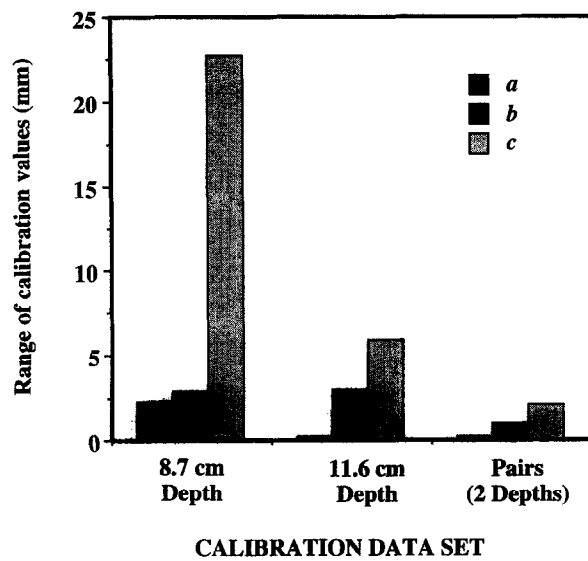


Fig. 9. Comparison of the ranges of the calibration matrix position components (*a*, *b*, *c*) for three subsets of calibration data. The calibration sets represent three image sets collected with the smaller container (8.7-cm imaging depth), three with the larger container (11.6-cm imaging depth) and three independent pairs of image sets collected at different depths. The position components represent the offset between the image plane origin and the receiver origin (*S* in Fig. 3b). The range is the difference between the maximum and minimum value returned for each translational component by the three calibration runs performed on each set. The variability in the calibration algorithm output was reduced when data from different imaging depths were combined.

as the complexity of the scanning protocol increased. The rms uncertainty increased from 0.7 to 0.9 mm when a 90° transducer rotation was introduced at a single imaging window, but increased to 2.0 mm with a change in viewing location from the *x*- to the *y*-axis (protocol 3).

Imaging precision as a function of target distance from the transmitter is shown in Fig. 12. For one window and scanhead orientation, the rms uncertainty varied from 0.6 mm to approximately 1 mm over the system's range of operation.

Imaging precision as a function of target distance from the scanhead face is shown in Fig. 13. For one viewing window and scanhead orientation, the rms uncertainty varied from 0.5 mm to approximately 1 mm over an imaging depth from 4–15 cm.

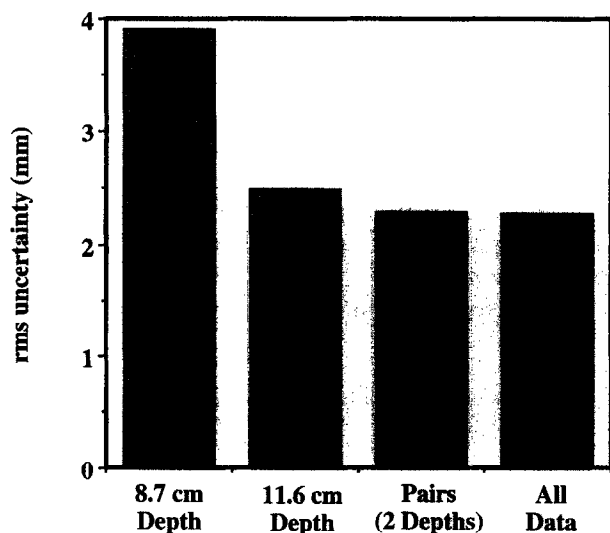
**Accuracy.** The mean error in measured distance between beads was < 0.1 mm for both imaging depths ( $0.04 \pm 0.67$  mm at 8.7-cm depth,  $0.09 \pm 0.69$  mm at 12.4-cm depth). Imaging accuracy as a function of target distance from the transmitter is shown in Fig.

14. The mean difference from the true distance was < 1 mm over the operating range of the system.

## DISCUSSION

The overall performance of the miniature magnetic sensor compares well with that of the standard-sized sensor. According to the manufacturer, the miniature sensor is accurate to 0.8 mm rms in position and 0.18° rms in angle when it operates within 50 cm of the transmitter. The manufacturer's accuracy specifications for the standard sensor are 0.9 mm and 0.15°, valid over a larger range (91 cm). The measured precision of the miniature sensor over its rated operating range was 1.7 mm, while the precision for the standard sensor over its larger operating range was 1.6 mm. In ultrasound imaging tests, the overall rms uncertainty in point location was 2.4 mm for the miniature sensor and 2.1 mm for the standard sensor.

The measured precision of both the miniature and standard magnetic sensors was better than results previously reported by Detmer *et al.* (1994). They found the mean rms uncertainty in point location to be 2.5



## CALIBRATION DATA SET

Fig. 10. Comparison of imaging precision using calibration matrices derived from the three data subsets of Fig. 9 and the overall calibration matrix (derived from all six data sets). Each matrix was used to find the rms uncertainty in point location for eight independent image sets, and the results were averaged. Each of the first three columns (left to right) represents the average precision for the three calibration matrices in each set; the last column is the performance of the final calibration matrix. The precision improves when data from different imaging depths are combined to calculate the calibration matrix.

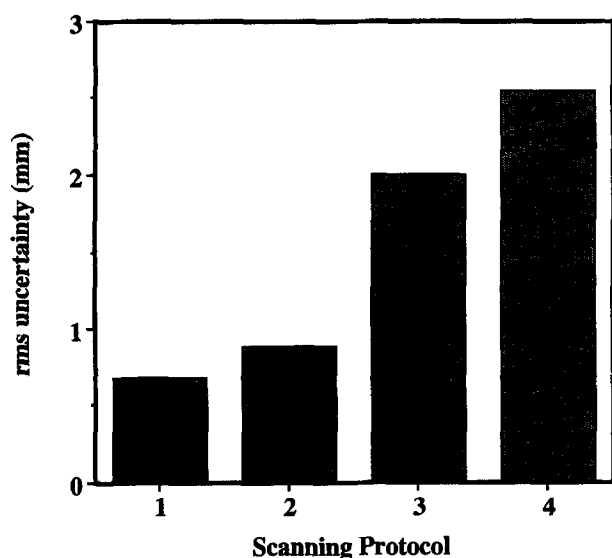


Fig. 11. Comparison of precision for simulated imaging protocols. The rms uncertainty increases as the complexity of the imaging protocol increases. The rms uncertainty in point target location is  $< 1$  mm when imaging from a single window (Protocols 1 and 2). The final calibration matrix was used in all cases to compute the target location. Protocol 1 = one imaging window with a single scanhead orientation; Protocol 2 = one imaging window with two scanhead orientations; Protocol 3 = two imaging windows with two scanhead orientations; Protocol 4 = arbitrary imaging windows and scanhead orientations.

mm for the sensor alone and 3.0 mm for the ultrasound imaging system. For the sensor alone, the difference in results between the earlier and present studies is due to the manufacturer's improvements in the magnetic location system itself. Note, however, that different scanheads were used in the imaging tests (7.5-MHz

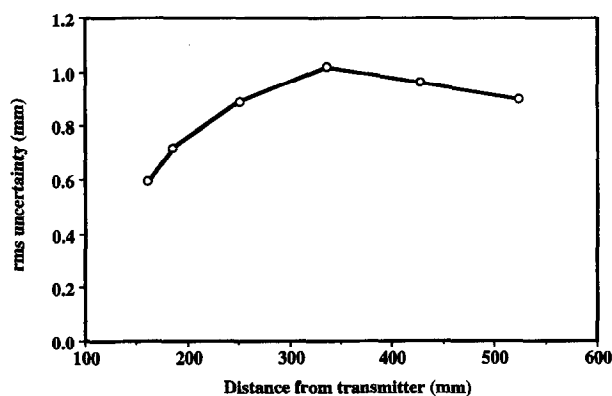


Fig. 12. Imaging precision as a function of target distance from the transmitter for imaging from one window with one scanhead orientation. Sixteen images were collected at each distance.

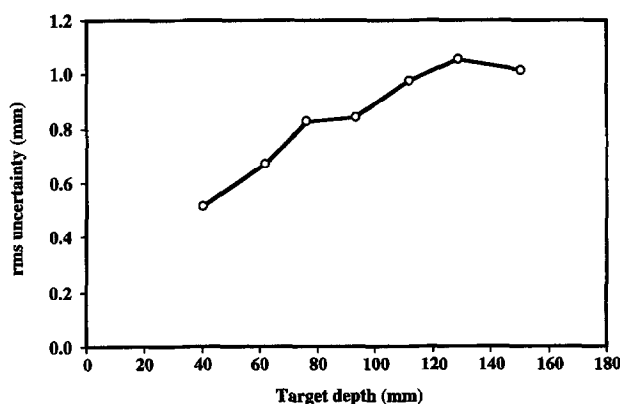


Fig. 13. Imaging precision as a function of target depth for imaging from one window with one scanhead orientation. Sixteen images were collected at each depth setting. The rms uncertainty increases as the target's distance from the scanhead face increases.

linear array in the earlier study, 5- to 3-MHz sector scan in the present study). While both the sensor and the calibration procedure were refined in the present study, direct comparison of the results is complicated by differences in ultrasound resolution and beam shape.

The miniature magnetic sensor proved to be insensitive to electromagnetic interference and noise from nearby circuits. Preliminary stylus tests of the sensor, both with and without an ultrasound scanhead attached, indicated no increase in measurement error due to conductors within the scanhead. All subsequent tests of the magnetic locating system alone were performed with the sensor mounted on the ultrasound scanhead. In addition, the system's accuracy and precision were

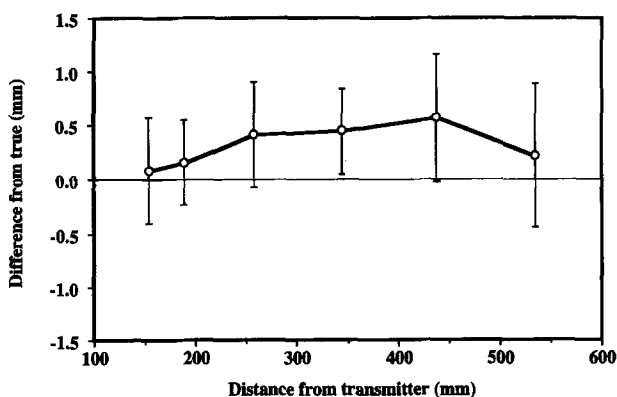


Fig. 14. Mean difference between the length measured by imaging and the true length as a function of target distance from the transmitter for images of a grid of beads. The bars represent the standard deviations for 10 measurements at each distance.

not sensitive to ultrasound instrument operation. Therefore, imaging can be performed with the sensor mounted directly on (or even within) the scanhead, minimizing the distance from the receiver to the transducer face. Since angle errors are magnified by the distance from the sensor to the target (Detmer *et al.* 1994), the effect of noise and calibration uncertainty on image reconstruction is reduced. The effect of imaging depth on precision is quantified in Fig. 13. As expected, uncertainty in point location increased with the depth of the target, most likely due to both decreased imaging resolution and increased sensor angle measurement errors.

While magnetic systems are known to be susceptible to interference from metals, it was shown that the system performance varies with the type of metal present. Ferromagnetic materials such as carbon steel or iron will distort the magnetic fields and introduce errors regardless of the system measurement rate. Low-permeability, low-conductivity metals such as stainless steel do not introduce errors in the tracking system at either a high or a low measurement rate. If aluminum (low permeability, high conductivity) is present, the measurement rate and filtering parameters can be adjusted to minimize its effect on performance. Note, however, that a lower measurement rate can produce a lag in the tracking of rapid sensor movements. If the scanhead remains stationary during image acquisition (during *in vitro* tests for instance), a lower measurement rate is acceptable. If the scanhead moves during acquisition, as in a continuous scan of a heart *in vivo*, a higher sampling rate is preferred to accurately track the movement of the scanhead over time. Note also that system performance degrades somewhat for lower measurement rates, likely due to the manufacturer's optimization for higher operating rates.

The tests that were performed with the magnetic sensor alone establish the limits in point location precision and accuracy that can be expected of the system. Use of the location sensor in conjunction with an ultrasound probe introduces additional uncertainty in the location of a point in an ultrasound image, due to such factors as ultrasound lateral and axial resolution, ultrasound beam thickness and identification of the point of interest in the image (either manually or by computer). In the range for which imaging tests were conducted (15–30 cm), the rms uncertainty in point target location was 1.7 mm for the magnetic sensor alone, compared with 2.4 mm with the imaging system.

The accuracy of the imaging calibration procedure is related to the ultrasound image resolution. The position offsets depend on accurate location of the point target in multiple images. The magnetic sensor was

mounted on the scanhead such that the *a*-axis was aligned with the axial beam direction (image row), the *b*-axis was aligned with the lateral beam direction (image column) and the *c*-axis was aligned with the out-of-plane beam thickness (Fig. 1). Using bead targets embedded in gelatin, the resolution of the scanhead was found for an imaging depth of 8.7 cm (1.1-mm axial resolution, 2.8-mm lateral, 5.2-mm thickness) and for an imaging depth of 11.6 cm (1.2-mm axial resolution, 3.9-mm lateral, 5.2-mm thickness). Measurements were made along the centerline of the image sector proximal to the focus and represent the full-width at half-maximum of the image intensity. The order of decreasing image resolution (axial, lateral, thickness) corresponds to the order of increasing calibration variability (*a*, *b*, *c*) shown in Fig. 9.

Calibration accuracy is also sensitive to the range of target positions sampled within the image plane. While the target reconstructs to a single point in the transmitter coordinate system, the multiple target measurements lie in a plane in the receiver coordinate system. The calibration algorithm effectively searches for the plane that best fits the set of imaged points. A greater distribution of points in the image coordinate system (row and column locations) results in a better-defined plane and a more accurate calibration matrix. For a typical calibration imaging run, the range of point positions was 40 mm laterally (along the image rows) but only 12 mm axially (along the image columns). The smallest axial target range was 8.5 mm, for one calibration data set from the smaller cylinder. This set produced a particularly inaccurate calibration matrix, resulting in the large *c*-component range observed at the 8.7-cm imaging depth in Fig. 9. The combined data from different imaging depths had an overall target axial range of approximately 50 mm, resulting in the reduced calibration variability observed for the paired data sets.

Accurate calibration also depends on imaging with a wide range of transducer positions and orientations. If a large volume is sampled during calibration, a best-fit matrix for arbitrary imaging protocols can be calculated. This matrix compensates for nonuniform system response in the volume surrounding the transmitter. If imaging tests will be performed only in a well-defined region of the transmitter coordinate system (the *+x/+y* quadrant, for instance), then transducer positioning can be restricted to this region during calibration. However, imaging in other regions may be subject to larger 3D location errors.

Evidence of systematic measurement errors was observed during calibration of the location system. Correlation between the receiver location and the com-

puted 3D target position was found, particularly between the  $x$ - and  $y$ -components. These dependencies appear to be a characteristic of the magnetic location system and account for approximately half of the rms uncertainty in point target location when imaging is performed from multiple viewing windows. This effect was apparent when precision results were compared for different scanning protocols (Fig. 10). While changes in transducer orientation at a single imaging window had a minor effect on the rms uncertainty, the addition of a second viewing window approximately doubled the error. Preliminary work has indicated that corrections can be computed and applied to the data to improve performance. A regression applied to the calibration data set (Table 1) reduced the overall rms uncertainty from 2.4 to 1.6 mm. Some of the systematic error may be due to an assumption that the magnetic field generator is a point source when the system calculates the receiver position. This approximation breaks down near the transmitter, and the manufacturer recommends operation beyond a range of 350 mm to minimize systematic errors. This issue is being investigated further.

Given some degree of nonuniformity in system response, the performance for a given imaging application improves when transducer movement is minimized. Most ultrasound imaging protocols include some limits on transducer movement, often due to anatomical restriction of acoustic viewing windows. For example, transthoracic imaging windows for the heart are constrained by the ribs and the lungs. A cardiac imaging protocol including parasternal long- and short-axis views and an apical view typically requires a range of transducer movement of only 15 cm. In addition, the transducer generally maintains a single viewing direction relative to the transmitter. For practical imaging situations such as these, the rms uncertainty in point location can be  $< 1$  mm, which makes the performance comparable to that reported for optical, acoustic and mechanical locating systems (King et al. 1991; Martin et al. 1990; Trobaugh et al. 1994).

## SUMMARY

We analyzed the performance of a miniature magnetic position and orientation sensor for 3D ultrasound imaging and highlighted several aspects of system configuration and operation that can improve the overall performance. The locating system was not sensitive to ultrasound instrument operation or to conductors in the imaging scanhead, which permits direct mounting of the sensor on the scanhead. While the system is not sensitive to stainless steel in the vicinity, ferromagnetic

materials should not be brought within close proximity of the sensor or transmitter. Aluminum and similar low-permeability/high-conductivity metals can be introduced in the environment if a lower sensor measurement rate can be tolerated. For accurate and consistent system calibration, images should be collected over a range of transducer positions, and the coordinates of the imaged point should be widely distributed in the image plane. If possible, imaging should be performed at distances  $> 350$  mm from the transmitter, since systematic errors tend to increase in the near range.

The miniature magnetic sensor performed well both in comparison to a standard-sized sensor and to other 3D locating techniques reported in the literature. The precision and accuracy characterized in this study indicate that the miniature magnetic sensor is suitable for many ultrasound imaging tasks. In typical imaging applications with somewhat limited transducer movement, the system can locate a single point in an ultrasound image with rms uncertainty  $< 1$  mm. The small size of the sensor makes it particularly useful for procedures such as intraoperative and transesophageal imaging. Design improvements are expected to increase the sensor range and reduce systematic errors, which will increase its potential for clinical use.

**Acknowledgements**—This work was supported in part by grants from the National Institutes of Health (grants HL41464 and R43RR07741), Ascension Technology Corp. (Burlington, VT, USA) and Advanced Technology Laboratories, Inc. (Bothell, WA, USA).

## REFERENCES

- Delcker A, Diener HC. Quantification of atherosclerotic plaques in carotid arteries by three-dimensional ultrasound. *Br J Radiol* 1994;67:672–678.
- Detmer PR, Bashein G, Hodges T, et al. 3D ultrasonic image feature localization based on magnetic scanhead tracking: *In vitro* calibration and validation. *Ultrasound Med Biol* 1994;20:923–936.
- Gilja OH, Smievoll AI, Thune N, et al. *In vivo* comparison of 3D ultrasonography and magnetic resonance imaging in volume estimation of human kidneys. *Ultrasound Med Biol* 1995;21:25–32.
- Gilja OH, Thune N, Matre K, et al. *In vitro* evaluation of three-dimensional ultrasonography in volume estimation of abdominal organs. *Ultrasound Med Biol* 1994;20:157–165.
- Handschumacher MD, Lethor JP, Siu SC, et al. A new integrated system for three-dimensional echocardiographic reconstruction: Development and validation for ventricular volume with application in human subjects. *J Am Coll Cardiol* 1993;21:743–753.
- Hodges TC, Detmer PR, Burns DH, et al. Ultrasonic three-dimensional reconstruction: *In vitro* and *in vivo* volume and area measurement. *Ultrasound Med Biol* 1994;20:719–729.
- Jiang L, Vazquez de Prada JA, Handschumacher MD, et al. Quantitative three-dimensional reconstruction of aneurysmal left ventricles: *In vitro* and *in vivo* validation. *Circulation* 1995;91:222–230.
- Kelly IMG, Gardener JE, Brett AD, Richards R, Lees WR. Three-dimensional US of the fetus: Work in progress. *Radiology* 1994;192:253–259.
- King DL, King DL, Jr, Shao MY. Evaluation of *in vitro* measurement

- accuracy of a three-dimensional ultrasound scanner. *J Ultrasound Med* 1991;10:77–82.
- King DL, King DL, Jr, Shao MY. Three-dimensional spatial registration and interactive display of position and orientation of real-time ultrasound images. *J Ultrasound Med* 1990;9:525–532.
- Leotta DF, Detmer PR, Gilja OH, et al. Three-dimensional ultrasound imaging using multiple magnetic tracking systems and miniature magnetic sensors. In: *Proceedings IEEE International Ultrasonics Symposium*. 1995;1415–1418.
- Martin R, Blood E, Sheehan F, et al. A miniature position and orientation locator for three dimensional echocardiography. In: *Proceedings Computers in Cardiology*. 1993;25–28.
- Martin RW, Bashein G, Detmer PR, Moritz WE. Ventricular volume measurement from a multiplanar transesophageal ultrasonic imaging system: An *in vitro* study. *IEEE Trans Biomed Eng* 1990;BME-37:442–449.
- Pretorius DH, Nelson TR. Prenatal visualization of cranial sutures and fontanelles with three-dimensional ultrasonography. *J Ultrasound Med* 1994;13:871–876.
- Riccabona M, Nelson TR, Pretorius DH, Davidson TE. Distance and volume measurement using three-dimensional ultrasonography. *J Ultrasound Med* 1995;14:881–886.
- Roelandt JRTC, ten Cate FJ, Vletter WB, Taams MA. Ultrasonic dynamic three-dimensional visualization of the heart with a multiplane transesophageal imaging transducer. *J Am Soc Echocardiogr* 1994;7:217–229.
- Sapin PM, Schroeder KD, Gopal AS, et al. Comparison of two- and three-dimensional echocardiography with cineventriculography for measurement of left ventricular volume in patients. *J Am Coll Cardiol* 1994;24:1054–1063.
- Sapin PM, Schroeder KD, Smith MD, DeMaria AN, King DL. Three-dimensional echocardiographic measurement of left ventricular volume *in vitro*: Comparison with two-dimensional echocardiography and cineventriculography. *J Am Coll Cardiol* 1993;22:1530–1537.
- Stone M. A three-dimensional model of tongue movement based on ultrasound and x-ray microbeam data. *J Acoust Soc Am* 1990;87:2207–2217.
- Trobaugh JW, Richard WD, Smith KR, Bucholz RD. Frameless stereotactic ultrasonography: Method and applications. *Comp Med Imaging Graphics* 1994;18:235–246.